Unique characteristic features of stimulated Brillouin scattering in small-core photonic crystal fibers

John E. McElhenny,[1] Radha K. Pattnaik,[1] Jean Toulouse,[1,*] Kunimasa Saitoh,[2] and Masanori Koshiba[2]

[1]*Department of Physics, Lehigh University, Bethlehem, Pennsylvania 18015, USA*
[2]*Graduate School of Information Science and Technology, Hokkaido University, Sapporo 060-0814, Japan*
**Corresponding author: jt02@lehigh.edu*

Received August 23, 2007; revised January 14, 2008; accepted January 21, 2008;
posted January 30, 2008 (Doc. ID 86782); published March 26, 2008

We present extensive stimulated Brillouin scattering (SBS) results from experiments and modeling for four different photonic crystal fibers (PCFs) with core diameters ranging from 8 to 1.7 μm. These results reveal several SBS characteristic features of small-core PCFs, high thresholds, and acoustic peaks, which are due to their antiguiding nature and highly multimode acoustic character. The nature of what we believe to be new acoustic modes is examined in the light of the large variations observed in the Brillouin gain, Brillouin threshold, and Brillouin shift with decreasing core diameter and optical wavelength. © 2008 Optical Society of America

OCIS codes: 290.5830, 060.5295.

1. INTRODUCTION

Stimulated Brillouin scattering (SBS) arises from the interaction between an optical and an acoustic wave. Naturally, the strength of this interaction is strongly dependent upon the degree of overlap between the two waves, thereby determining the Brillouin gain and the threshold power at which the scattering becomes stimulated. In conventional single-mode fibers (SMFs), both the optical mode and the acoustic wave are guided and the modes overlap in the core of the fiber, because both the optical and effective acoustic refractive indices are higher in the Ge-doped silica core. Consequently, the Brillouin gain is large and the threshold power relatively low. The situation appears to be very different in photonic crystal fibers (PCFs), for several reasons. First, the optic mode is not exactly circular Gaussian but spreads out between the holes and into the cladding. The degree to which the optical wave extends out also depends on the wavelength. Second, unless there would be a bandgap effect, PCFs should behave as acoustic antiguides because the effective acoustic index is significantly lower in the holey cladding than in the core. In other words, the waveguide for the acoustic modes will be the entire holey cladding. This should definitely reduce the degree of overlap of the optical and acoustic waves, reducing the SBS gain and raising the threshold accordingly. Third, as the core size decreases, it will behave more and more as a point source for the generation of the acoustic waves, which will consequently no longer be generated simply as plane waves but more like semi-radial waves. For these reasons, SBS in PCFs can be expected to display new and interesting characteristics. This should be all the more visible in PCFs with a small core and/or a large numerical aperture (NA). Several short papers have already appeared on the subject of SBS in PCFs, each reporting measurements on a specific fiber. In a Blaze Photonics PCF, Texier *et al.* [1] observed that the threshold for SBS was higher than in conventional SMFs and also that efficient lasing was induced by the stimulated scattering. Zou and co-workers [2] measured SBS in a PCF with a Ge-doped core and showed that it consisted of one main peak and several smaller peaks. They also reported on the evolution of these peaks with temperature. Dainese *et al.* [3] also reported Brillouin results, suggesting the existence of additional peaks in small-core PCFs, although the spectrum shown was for spontaneous Brillouin in the forward direction. On the simulation side, Saitoh and Koshiba [4] and Laude *et al.* [5] studied the fundamental characteristics of localized acoustic modes in PCFs. In the present paper, we report the results of a more comprehensive SBS experimental and theoretical study of several different PCFs and identify a trend for SBS in fibers with different hole diameters, d_H, different pitches, Λ, and, accordingly, different core sizes, d_C. In the first part of the paper we present the experimental Brillouin results obtained on these fibers. In the second part, we present the simulation results for the corresponding fibers, and in the third part we compare and discuss both sets of results and draw general conclusions as to the unique characteristics of SBS in PCFs and, in particular, the nature of the new SBS peaks observed.

2. FIBER STRUCTURE, PARAMETERS, AND CALCULATED STIMULATED BRILLOUIN SCATTERING THRESHOLD

Four different PCFs were studied in the present work: (i) RB61 from OFS (d_C=8 μm, Λ=4.9 μm, and d_H=1.85 μm with five layers); (ii) PC421 from Blaze Photonics (d_C =5.2 μm, Λ=3.4 μm, and d_H=1.8 μm with five layers);

Table 1. Fiber Parameters at 1550 nm and Threshold SBS Powers Calculated Using Eq. (1), Assuming a Brillouin Coefficient $g_B = 5 \times 10^{-11}$ W/m

Fiber	d_c (μm)	α (dB/km)	L (m)	L_{eff} (m)	$A_{\text{core}}^{\text{opt}}$ (μm^2)	$A_{\text{eff}}^{\text{opt}}$ (μm^2)	$A_{\text{eff}}^{\text{ao}}$ (μm^2)	$P_{\text{th}}^{\text{opt}}$ (dBm)	$P_{\text{th}}^{\text{ao}}$ (dBm)
RB61	8	2	495	443	50.26	45.6	113	16.4	20.3
PC421	5.2	3	500	423	21.24	17.5	112	12.4	20.5
RB65	3.55	19.4	400	187	9.89	10.3	45.5	13.6	20.1
CF	1.7	71	390	61	2.27	4.0	21.6	14.4	21.7

(iii) RB65 from OFS ($d_C = 3.55\ \mu$m, $\Lambda = 2.35\ \mu$m, and $d_H = 1.15\ \mu$m with six layers); and (iv) a crystal fiber (CF) ($d_C = 1.7\ \mu$m, $\Lambda = 1.2\ \mu$m, and $d_H = 0.72\ \mu$m with ten layers). The core diameter is estimated from the relation $d_C = 2\Lambda - d_H$, where Λ is the lattice pitch (the distance from one air hole to the adjacent one, center to center) and d_H is the diameter of each air hole. When describing PCFs, an important quantity is the ratio d_H/Λ, which is related to the optical NA of the fiber. It may be useful to note that the value of the ratio d_H/Λ increases monotonically with decreasing core size for the fibers studied. The Blaze Photonics fiber deviates slightly from this monotonic trend, and its main SBS peak has a slightly different shape [1]. However, its SBS parameters still follow reasonably well the trends presented here for the three others fibers that are the main focus of the present paper. Simulations using both beam propagation (BEAMPROP) and finite element (FEMSIM) software have shown all four fibers to be single mode. The effective areas of the modes are given by [6]

$$A_{\text{eff}}^{\text{opt}} = \frac{\left(\int\int |F(x,y)|^2 \mathrm{d}x\mathrm{d}y \right)^2}{\int\int |F(x,y)|^4 \mathrm{d}x\mathrm{d}y}, \tag{1}$$

where $F(x,y)$ is the modal distribution of the fundamental fiber mode. These results are included in Table 1.

One of the main characteristics of a fiber, and an essential one in determining the SBS threshold, is its attenuation or loss. The SBS threshold depends on the attenuation through the effective length, $L_{\text{eff}} = \alpha^{-1}[1 - \exp(-\alpha L)]$, and is usually given by the simple expression [6,7]

$$P_{\text{th}} = 21 \frac{A_{\text{eff}}}{g_B L_{\text{eff}}}. \tag{2}$$

This simple expression for the threshold implicitly assumes a 100% overlap between the optic and the acoustic modes, a condition that is not satisfied in PCFs, as will become apparent below. The attenuation of the four fibers was measured using the cut-back technique. The RB61 fiber, being closer to an SMF, exhibited a lower loss of about 2 dB/km and did not show a strong wavelength dependence in the narrow range of wavelengths investigated. The PC421 fiber had a slightly higher loss of 3 dB/km, which decreased slightly with increasing wavelength. The loss in the other two fibers was significantly higher ($\geqslant$20 dB/km) and exhibited a strong wavelength dependence, shown in Fig. 1. The difference between the last two fibers was a much higher loss in the CF than in the RB65 fiber and an opposite wavelength dependence, the loss decreasing with wavelength in RB65 but increasing with wavelength is the CF. This difference may be attributable in part to the fact that the optical mode in the CF extends into the holey cladding, as indicated by the simulations below.

Next, we examine the degree of confinement of the optical wave in the two smallest core fibers, the RB65 and CF. This is essential because the strength of SBS acutely depends on the overlap between the optical and acoustic waves, and because, as was mentioned earlier, the acoustic wave in PCFs will tend to propagate in the holey cladding. In Fig. 2 we compare the effective area of the optical mode and the geometrical core area as a function of core diameter for values of d_H/Λ corresponding to those of the CF and RB65 fibers, 0.6 and 0.49, respectively. In both

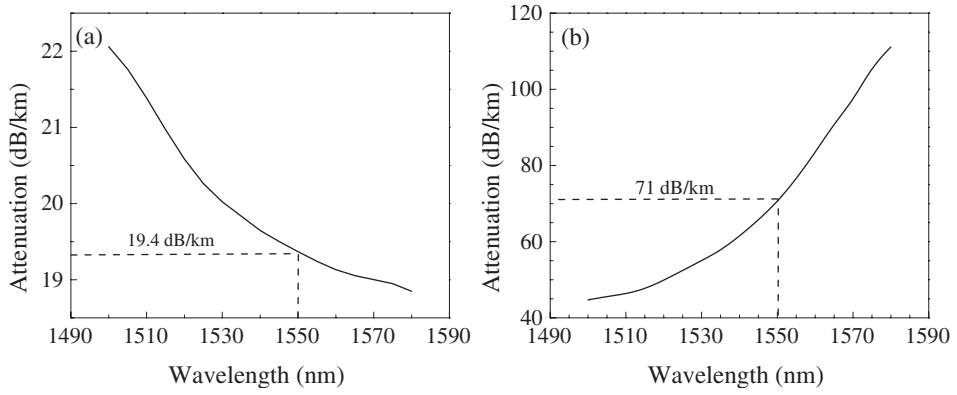

Fig. 1. Measured attenuation (using cut-back technique) in the small-core (a) RB65 fiber and (b) crystal fiber. Note that the attenuation in both fibers is in excess of 20 dB/km at 1550 nm.

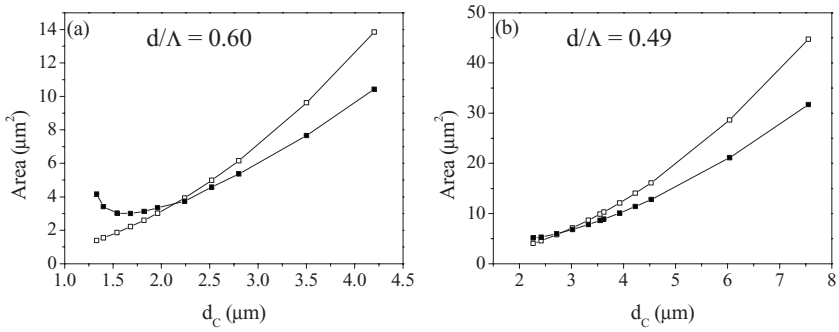

Fig. 2. Effective area of the optical mode (solid) and geometric core area (open) as a function of core size for a d/Λ of (a) 0.60 matching that of the CF and (b) 0.49 matching that of the RB65 fiber.

plots we note that, below a certain core diameter, or above a certain d_H/Λ ratio, the effective area of the mode exceeds the geometrical area of the core, which should affect the SBS behavior. With core diameters of 3.55 μm and 1.7 μm, respectively, we see that the optical mode is still confined within the core in the RB65 fiber while it extends into the holey cladding in the CF.

The loss and the effective length measured at the 1550 nm wavelength and the calculated Brillouin threshold are given in Table 1 for the different fibers studied. Here, the Brillouin threshold is calculated using both the effective area of the optical mode, $A_{\text{eff}}^{\text{opt}}$, and the acousto-optic effective mode area, $A_{\text{eff}}^{\text{ao}}$, defined later in the paper.

It is interesting to note that, according to the simple expression for the SBS threshold and using the effective area of the optical mode, the CF would be expected to have the lowest threshold, when in fact the opposite was observed (see below). However, the proper trend is observed when using the acousto-optic effective mode area instead of simply the effective area of the optical mode.

3. BRILLOUIN SCATTERING SETUP

Brillouin scattering was measured by using a self-heterodyne technique, and the setup is shown in Fig. 3. A signal from a Photonetics external cavity laser (ECL) was split by a 3 dB coupler and then amplified by a 30 dB gain optical amplifier (IPG Photonics' erbium fiber amplifier model EAD-1-C) before being injected into the test fibers through a polarization controller in order to investigate the pump polarization dependence of the Brillouin gain. The other half of the signal (from the ECL), used as the local oscillator, was amplified and mixed with the backscattered Stokes light from the fiber for heterodyne detection.

The spectrum of the backscattered light was recorded by using an electrical spectrum analyzer (ESA), and the integrated power was simultaneously measured with an optical power meter. In parallel, a high-resolution optical spectrum analyzer with a resolution bandwidth of 0.05 nm was used to record the Brillouin signal as a function of input power. These measurements were made for four different wavelengths, 1535, 1540, 1550, and 1560 nm, of the input pump beam. The choice of wavelength was constrained by the bandwidth of the amplifier, from 1535 to 1565 nm. All measurements were taken over the input power range from 14 to 30 dB m.

4. BRILLOUIN SCATTERING RESULTS

SBS in fibers is normally characterized by a threshold, a Brillouin shift, and the magnitude of the Stokes or backscattered power and, obviously, also depends on the specific acoustic modes involved. Two separate types of measurements were performed on the four fibers presented above. First, the transmitted and backscattered powers were measured with a power meter and, second, the Brillouin spectrum was measured on the setup described above. In the following, we successively examine in some detail the results obtained on three of the fibers, RB61 with a core diameter of 8 μm, RB65 with a core of 3.55 μm, and CF with a core diameter of 1.7 μm. The results on the fourth fiber, PC421 from Blazed Photonics with a 5.2 μm core, were published earlier [1] and are only included in the summary graphs later.

A. RB61 Fiber

The transmitted and reflected powers are shown in Fig. 4 for the 1550 nm wavelength. Both increase almost linearly with pump power up to the SBS threshold of about

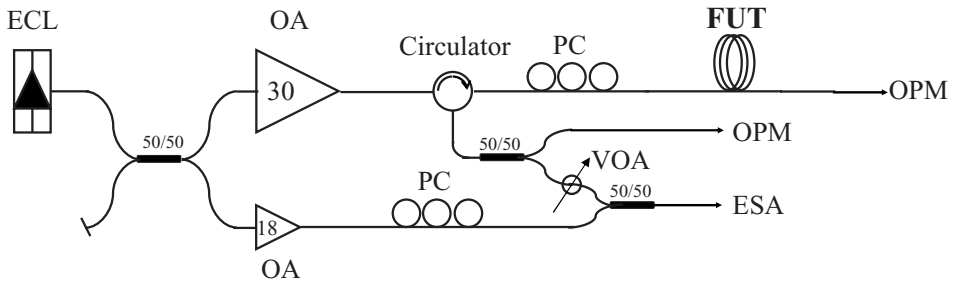

Fig. 3. Schematics of the Brillouin scattering measurement setup.

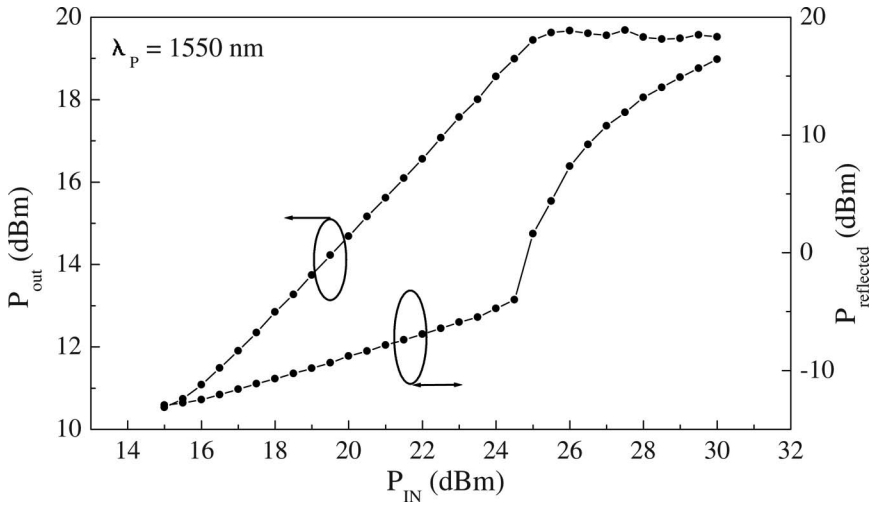

Fig. 4. Output and reflected power in the large-core RB61 fiber. The Brillouin scattering becomes stimulated when the input power exceeds 24 dB m.

25 dB m. In this larger core fiber, the threshold did not exhibit any significant wavelength dependence. As expected beyond the threshold, the reflected power increases by more than 20 dB and the transmitted power saturates.

It is important to note that the input powers indicated in Fig. 4 correspond to powers that were measured at the output of the optical amplifier. In order to obtain the actual powers launched into the fiber, one must estimate the extraneous losses from the circulator and splices. From the linear dependence of the transmitted power at low input powers (Rayleigh and spontaneous Brillouin range), we estimate the total average loss to be between 5 and 5.5 dB. With an intrinsic attenuation of about 1 dB through 495 m of the RB61 fiber and an insertion loss of the circulator of about 1 dB, the splice loss can then be estimated to be between 1.5 and 1.75 dB per splice. Subtracting the circulator and the splice losses from the observed threshold yields an estimate of 24.5−2.75 =21.75 dB m for the intrinsic threshold power. This is approximately 5 dB higher than the theoretical estimate based on the effective area of the optical mode, but only 1−2 dB lower than the estimate based on the acousto-optic effective mode area. The Brillouin spectrum of the RB61 fiber is shown in Fig. 5 for different input powers of the pump at 1550 nm. A single peak is observed with a Brillouin shift of 11.1 GHz, which is only slightly lower than the 11.4 GHz reported by Yeniay *et al.* [8] for a conventional single-mode silica fiber (All Wave from OFS, Inc.). Given the pure silica core and lower refractive index in the holey cladding of PCFs, a slightly lower Brillouin shift in the RB61 fiber can be expected.

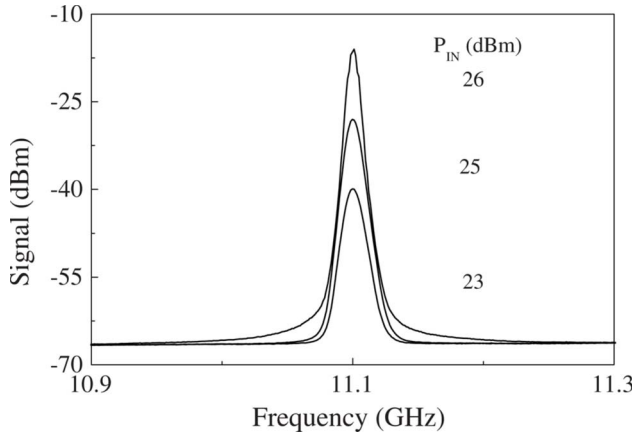

Fig. 5. Brillouin spectrum of the RB61 fiber with pump wavelength at 1550 nm for different input powers. The spectral shape is symmetric and does not reveal any unusual features. The peak is at 11.1 GHz.

The Brillouin spectrum of RB61 does not reveal any feature that would otherwise be strikingly different from that of a SMF. The spectral shape of the Stokes peak is quite symmetric, the gain increases with pump power, and it does not depend on the input polarization of the pump.

Since the Brillouin frequency shift is related to the pump wavelength by [8]

$$\nu_B = \frac{2n_{\text{eff}}V_A}{\lambda}, \tag{3}$$

in which n_{eff} is the effective optical refractive index and V_A is the acoustic velocity, the slope of the curve ν_B versus $1/\lambda$ should be equal to $2n_{\text{eff}}V_A$. If the index n_{eff} is known, one can estimate the acoustic velocity V_A.

As shown in Fig. 6, we estimate V_A in RB61 to be 5895 m/s (given a refractive index of 1.444 02 as per http://www.mellesgriot.com/products/optics/mp32.htm), which is almost exactly the velocity of longitudinal acoustic waves in bulk silica (5900 m/s) [9]. This agreement indicates that, because of the relatively large-core size of the RB61 fiber, the acoustic wave is mostly confined within the core of the fiber, as confirmed by the simulation results below.

B. RB65 Fiber

The reflected and transmitted powers for the RB65 fiber are shown in Fig. 7. As in the case of RB61, the powers indicated in this Fig. 7 are the output powers from the amplifier, and they need to be corrected for extraneous sources of loss present in the setup. After correction, the true Brillouin threshold for optimum polarization in

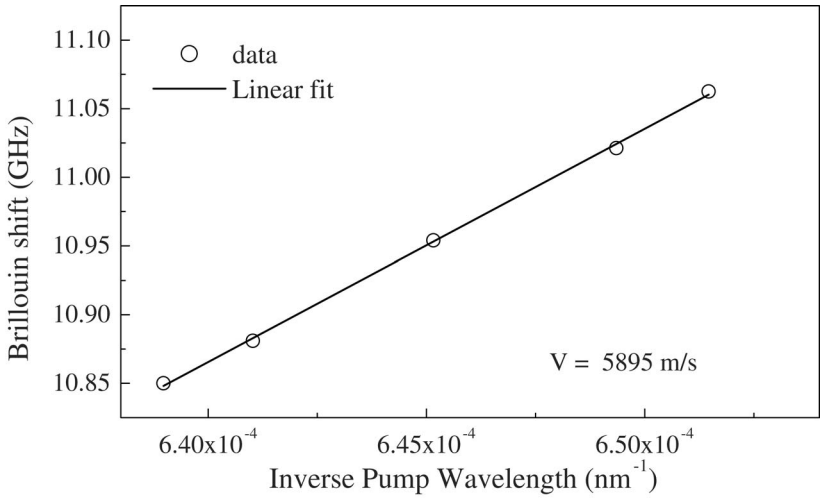

Fig. 6. Brillouin shift as a function of inverse pump wavelength. The speed of sound waves is estimated from the slope of the linear fit. A refractive index of 1.439 is assumed in this estimation.

RB65 is estimated to be about 18 dB m. This again is around 4.5 dB higher than the theoretical value (calculated using the effective area of the optical mode) given in Table 1, but only 2 dB lower than that calculated with the acousto-optic effective mode area.

The Brillouin spectrum from the small-core RB65 fiber is shown in Fig. 8. Unlike the threshold, the spectrum of RB65 is quite different from that of RB61 and exhibits unusual characteristics. As shown in Fig. 8, it consists of two peaks: the main peak and a second peak very close to it on the high-frequency side. Being on the high-frequency side, this second peak must be attributed to higher-order acoustic modes. Its origin will become clearer when comparing these results with those obtained on the smaller-core CF and by looking at the simulations results.

Next, the plot of ν_B versus $1/\lambda$ shown in Fig. 9 for RB65 shows two straight lines, corresponding, respectively, to the two Brillouin peaks observed in the spectrum. Using a finite element method (FEM) we determined the effective optical index to be 1.42. The slopes of these two straight lines in Fig. 9 then yield acoustic velocities of 6006 ± 20 m/s for the main peak and 3933 ± 200 m/s for the second peak. It is interesting to note at once that these velocities are typical of respective longitudinal and transverse acoustic waves in silica.

C. Crystal Fiber

The CF had the smallest core of the fibers studied. Despite its small core, we were still able to splice it to a SMF fiber, thus avoiding butt-coupling. The reflected and transmitted powers are shown in Fig. 10.

As was the case for the other fibers, the powers indicated are the output powers from the optical amplifier and do not correspond exactly to the actual powers launched into the fiber. The observed threshold must therefore be corrected for the extraneous losses present in the setup. After correction, the powers actually injected into the CF are estimated to be less than 4 dB (single splice loss) lower than the powers displayed in Fig. 10, placing the SBS threshold with an optimum state of polarization between 19 and 20 dB m. This value is again higher (5 dB) than the theoretical estimate obtained using the simple theoretical expression for the threshold

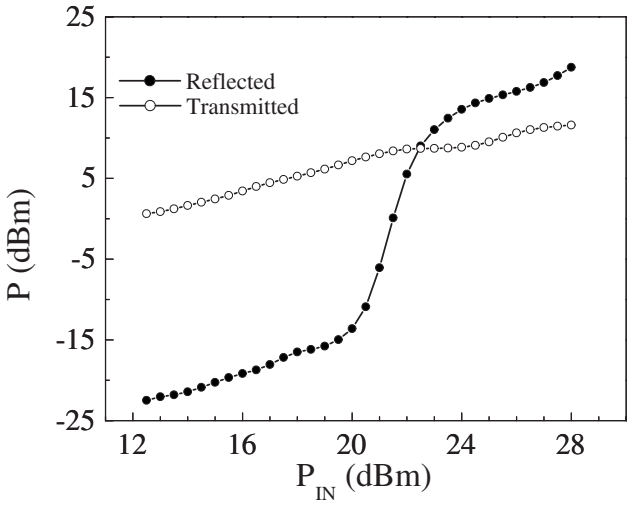

Fig. 7. Reflected (solid) and transmitted (open) power for RB65 fiber ($\lambda_P = 1550$ nm).

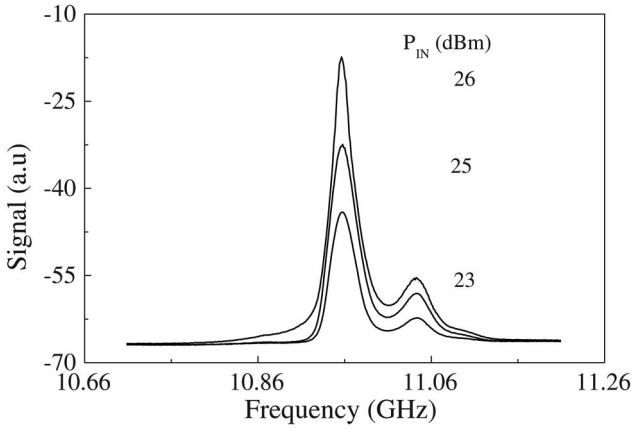

Fig. 8. Brillouin spectrum of the RB65 fiber with pump wavelength at 1550 nm. Signal for different input powers. The spectrum reveals an extra peak on the high frequency end. The main peak is at 10.96 GHz, while the second one is at 11.043 GHz.

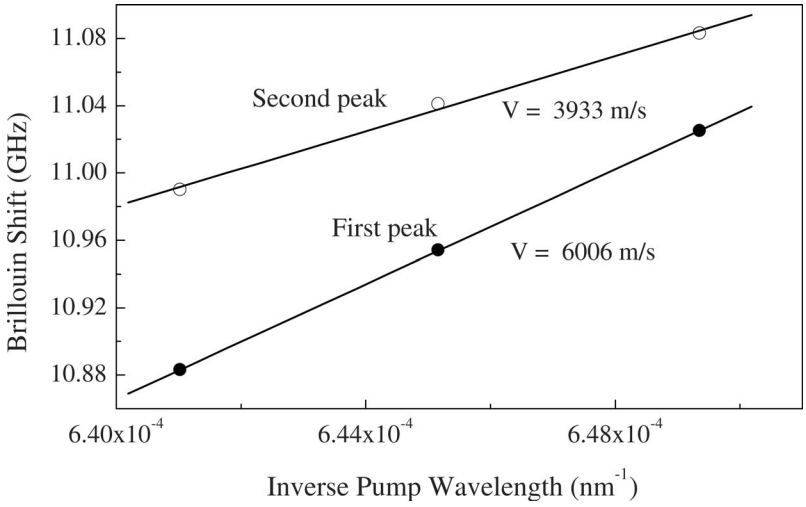

Fig. 9. Brillouin shift in RB65 fiber for different pump wavelengths. The speed of sound waves is estimated from the slope of the linear fit. An effective refractive of 1.42 was used in this estimation. A linear fit to the second peak curve does not pass through the origin.

and the effective area of the optical mode, but again is only about 2 dB lower than the theoretical value (21.7 dB m) calculated using the acousto-optic effective mode area. Having the highest threshold of the fibers points to an even-less-perfect overlap in the CF as well as antiguiding acoustic effects, an explanation that is borne out by the simulations below.

The Brillouin spectrum measured in the CF is presented in Fig. 11. As shown earlier, the attenuation in this CF was very high and increased with wavelength. Since the loss was lower at 1540 nm than at 1550 nm, we present the spectrum obtained with a 1540 nm pump, instead of 1550 nm as for the other fibers.

The spectrum now contains three peaks. In addition to a large main peak and a small second peak, a third peak is clearly observed approximately 400 MHz above the main peak. Furthermore, we observe that all three peaks go through the SBS threshold for the same input power. The same was also true of the second peak in RB65. In both cases, this suggests that the acoustic modes giving rise to the two or three Brillouin peaks are all simultaneously excited by the optical wave. An earlier paper by Dainese *et al.* [3] also reported additional peaks, albeit in the forward spontaneous Brillouin scattering of a 1.22 μm core fiber. It is worth mentioning that additional peaks are also observed in the spontaneous Brillouin spectrum of conventional fibers. In that case, however, they are due to leaky acoustic modes in the spontaneous regime and disappear in the stimulated range [8]. By contrast, in the PCFs studied here, these additional peaks grow with input launch power and are clearly a result of backward SBS.

In Fig. 12, we show the plot of ν_B versus $1/\lambda$. As for RB65, the slopes of the lines corresponding to the main and second peaks yield values of the acoustic velocities that are typical, albeit slightly smaller, than those of the respective longitudinal and transverse acoustic waves in silica. However, the slope of the line corresponding to the third peak yields an acoustic velocity (5259 m/s) that, surprisingly, is only slightly lower than the velocity of a longitudinal wave even though the Brillouin shift is greater than that of the main peak. Although this may be a coincidence, it might suggest that the third Brillouin peak somehow derives from the main peak or that the third peak is due to a higher-order acoustic mode.

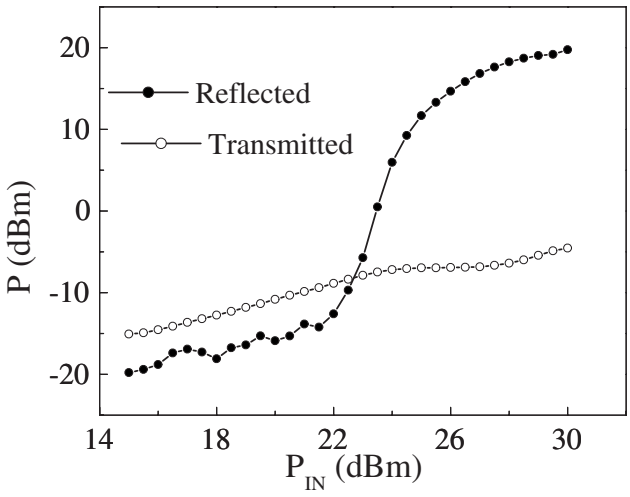

Fig. 10. Reflected (solid) and transmitted (open) powers in the CF (λ_P=1550 nm).

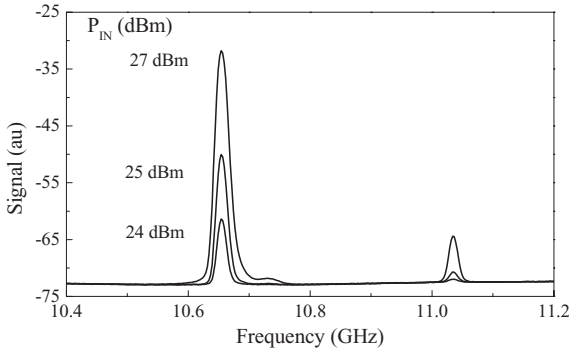

Fig. 11. Brillouin spectrum of the crystal fiber with pump wavelength at 1540 nm for different input powers. The spectrum reveals three peaks with the largest peak shifted to lower frequency, 10.65 GHz, the small second peak at 10.74 GHz, and the third peak at 11.04 GHz.

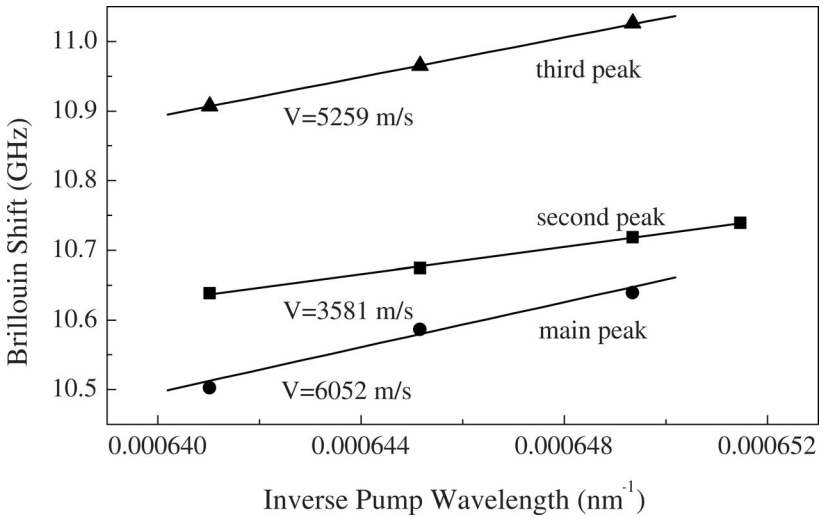

Fig. 12. Pump wavelength dependence of the Brillouin shift in CF. A linear fit to the first peak passes through the origin, as expected for longitudinal waves in solids. An effective refractive index of 1.359 was used in this estimation. A linear fit to the second peak, however, does not pass through the origin.

D. Summary of Stimulated Brillouin Scattering Results

1. Brillouin Threshold vs. Core Diameter

A comparison of the SBS threshold calculated from the simple Eq. (1) and that measured at the 1550 nm wavelength shows that the SBS threshold is significantly higher in PCFs than in conventional SMFs. To facilitate the comparison between the different fibers, in Fig. 13 we plot $21\times A_{\mathrm{eff}}(P_{\mathrm{th}}\times L_{\mathrm{eff}})^{-1}$, which should be equal to the Brillouin gain coefficient, g_{B}, according to the simple theoretical formula, Eq. (1).

The value of the Brillouin coefficient estimated from the threshold measurements falls well below the known value for bulk silica for the three larger-core fibers, and even much lower for the CF from (−3 to 6 dB). It is also worth noting that, for a given input pump polarization, the SBS threshold was observed to change by as much as 4 dB upon reversal of the fiber ends. Such an asymmetry was also observed with butt coupling and cannot be attributed to differences in splice losses at the two ends of the fiber. It must therefore be due to nonuniformity of the small-core CF and resulting nonuniformity in its birefringence. Mindful of this difference, all measurements reported in the present paper were done launching the pump from the same end of the fiber and tuning the polarization for maximum SBS.

2. Brillouin Shift vs. Core Diameter

A graphic summary of the position of the different Brillouin peaks, or Brillouin shifts, as a function of the core diameter is given in Fig. 14 for an optical wavelength of 1550 nm. As the core diameter decreases and d_H/Λ increases, the Brillouin shifts of both the main and second peaks together exhibit a precipitous drop similar to the dependence of the Brillouin gain coefficient seen in Fig. 13. It is interesting to note the similarities between this result and the Brillouin shift results reported by Yu *et al.* [10] on a triple-layer fiber (core–inner cladding–outer cladding), in which the inner cladding had a lower acoustic velocity and therefore a higher effective acoustic index than the two layers on either side of it.

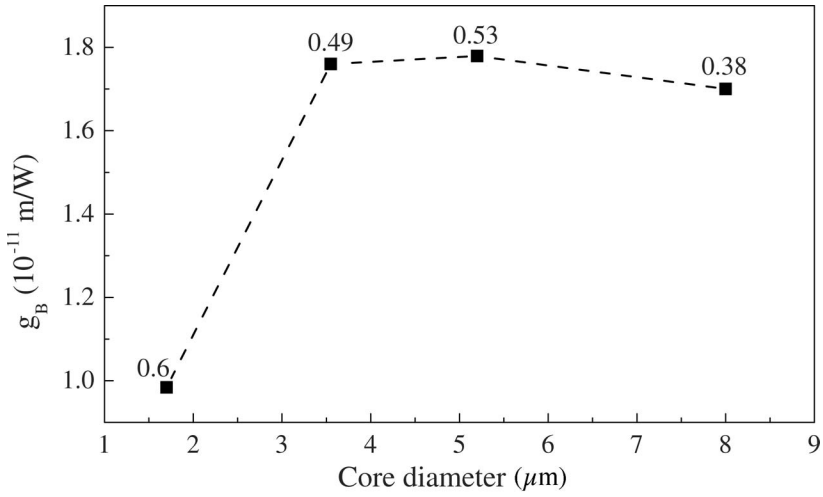

Fig. 13. Dependence of the Brillouin gain on core diameter. Values of the ratio d_H/Λ are indicated above each data point.

3. Wavelength Dependence

Although the range of wavelengths investigated was narrow (from 1535 to 1560 nm), the results clearly exhibited a wavelength dependence of the Brillouin threshold (not shown) as well as a wavelength dependence of the Brillouin shift. These were found to be particularly strong in the two smaller-core fibers, RB65 and CF. Two factors may have contributed to this wavelength dependence on the threshold. The first and most obvious one is the wavelength dependence on the loss (Fig. 1), and the second, which can be expected to play an important role in small-core PCFs, is the diffraction of acoustic waves by the lattice of air holes. The relative contributions of these two factors were not, however, resolved in the present study. The wavelength dependence of the Brillouin shift is expected and was used to determine the velocities of the corresponding acoustic modes (see ν_B versus $1/\lambda$ plots presented for each fiber). A puzzling observation there is that the curves corresponding to the second and third peaks do not extrapolate to zero at an infinite wavelength or zero wavevector, as one would expect for acoustic modes. One also notices a clear difference in the behavior of the different peaks. The second peak yields an acoustic velocity that is significantly lower than the acoustic velocity obtained from the main peak and is more typical of transverse modes in silica. By contrast, the third peak yields an acoustic velocity that is close to that obtained from the main peak, suggesting that the third Brillouin peak somehow derives from the main peak. These points are further addressed in Section 5.

E. Acoustic Simulations

In parallel with the experiments described above, we performed simulations of the acoustic modes in the three fibers under consideration, using a finite element model solver. In the following, we present a very brief overview of the model, and the results of the acoustic mode calculations, including the numerically calculated Brillouin gain spectrum (BGS) for the three PCFs under study.

1. Model

This model calculates the acoustic displacement distribution in the x, y, and z directions by solving the acoustic wave equation using an FEM algorithm. The details of the model were already given elsewhere [11]. The ith-order BGS, $g_i(f)$, is evaluated from the overlap between the acoustic mode field distribution $u_{zi}(x,y)$ and the optical LP_{01}-like mode field distribution $\phi(x,y)$ (major component of the electric field of the fundamental mode), and it is given by [12]

$$g_i(f) = \frac{4\pi n_{\text{eff}}^8 p_{12}^2}{\lambda^3 \rho c f_{Bi} \Delta f_{Bi}} \frac{\Delta f_{Bi}^2}{4(f - f_{Bi})^2 + \Delta f_{Bi}^2} \frac{1}{A_{\text{eff},i}^{\text{ao}}} \tag{4}$$

with the acousto-optic effective mode area

$$A_{\text{eff},i}^{\text{ao}} = \frac{\left[\int\int \phi^2(x,y)\mathrm{d}x\mathrm{d}y\right]^2}{\left[\int\int u_{zi}(x,y)\phi^2(x,y)\mathrm{d}x\mathrm{d}y\right]^2} \int\int u_{zi}^2(x,y)\mathrm{d}x\mathrm{d}y, \tag{5}$$

where p_{12} is the longitudinal elasto-optic coefficient, c is the velocity of light in vacuum, Δf_{Bi} is the full linewidth at half-maximum (FWHM) of the ith-acoustic mode, which is assumed to be the same $\Delta f_{Bi} \sim 40$ MHz for all modes, and $\phi(x,y)$ is the optical field distribution calculated by using a vector FEM [4] and confirmed with the FEMSIM program from RSoft, Inc. Since the acoustic modes are statistically independent, the total BGS is the sum of the BGS from each mode:

$$g(f) = \sum_i g_i(f). \tag{6}$$

It is important to note that the acousto-optic effective area is inversely proportional to the overlap integral over the optical and acoustic fields [see Eq. (5)]. Hence, a small acousto-optic effective area means a strong overlap between the optical and acoustic fields, which is not the case in PCFs.

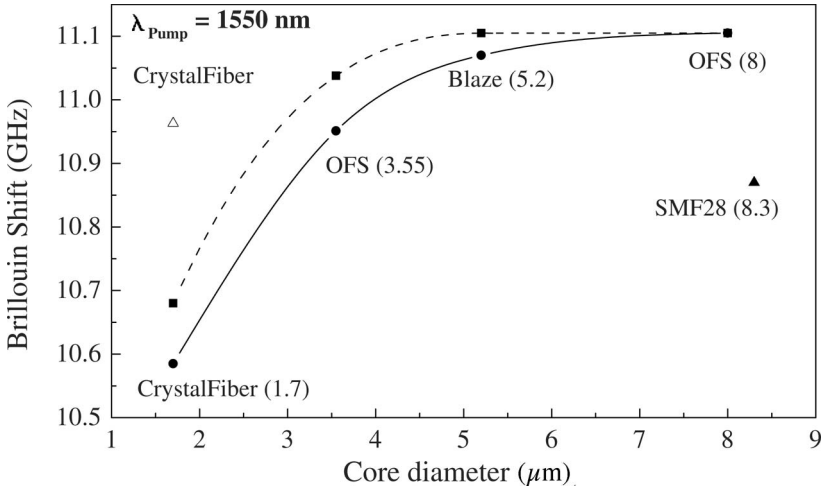

Fig. 14. Brillouin shift frequency as a function of core diameter. The connecting lines are a visual guide only. The solid curve shows the dependence of the main peak on the core size while the dashed curve shows the dependence of the second peak. The open triangle is indicates the frequency of the third peak of the CF.

2. Simulation Results

In Figs. 15(a)–15(c), we present the Brillouin gain curves calculated for the three main fibers used in the experiments at the 1550 nm wavelength. It is important to note that what is plotted in Fig. 15 is not the Brillouin coefficient but the Brillouin gain. Similar to the experimental results, RB61 exhibits only one major Brillouin peak, RB65 a second peak close to the main one, and CF a weak second peak close to the main peak and a third peak well separated from the main peak.

In Figs. 16(a)–16(c), we present the acoustic displacement distributions, $u_i(x,y)$ for the three main fibers discussed in this paper, RB61, RB65, and CF. For example, $u_z(x,y)$ represents the displacement amplitude in the z direction at a particular (x,y) point. It is important to note that these distributions represent the eigenvector of a particular propagating acoustic eigenmode of the fiber at a particular eigenfrequency. All calculations were carried out with at least six successive shells of holes, but only the central part of the calculation space is shown in the pictures for clarity. In Figs. 16(d)–16(f), we present the corresponding optical field distributions calculated using a FEM [13]. Figures 15 and 16 call for several remarks: (i) the fibers studied are clearly highly multimode acoustically, the modes being distributed over the entire core and holey cladding; these PCF fibers indeed tend to behave as acoustic antiguides. (ii) For the first two fibers, RB61 and RB65, the optical mode field and the acoustic displacement distributions overlap relatively well, but that is obviously not the case for the CF, for which the latter displacement distribution spreads out radially into the holey cladding.

We also calculated the x and y components of the acoustic displacement distribution and these are shown in Figs. 17(a)–17(d) for the CF at the frequencies of the main Brillouin peak and third peak (the second most prominent), respectively. For the third peak, we also include u_z for completeness. Although u_x and u_y are relatively small and evenly distributed at the first frequency (main peak), they are significant and nonuniform at the frequency of the third peak. This indicates that the third peak is not purely longitudinal but contains a nonnegligible torsional-radial component.

5. DISCUSSION

The results presented above demonstrate that PCFs behave very differently than SMFs with regard to SBS, and the smaller the core size the more significant this difference. The unique characteristics of PCFs are as follows:

- a SBS threshold that is higher in PCFs than in SMFs of equivalent core size;
- two or even three peaks observed in the backscattered stimulated Brillouin spectrum, with the frequency shift of the main and second peaks decreasing precipitously with decreasing core size;
- velocities derived from the first and second peak close to those of the respective longitudinal and transverse acoustic waves in silica, and velocity derived from the third peak only slightly smaller than that from the first peak; and
- shifts of the second and third peaks which, although approximately linear with inverse wavelength, do not extrapolate to zero for long wavelengths.

The simulation results presented in Subsection 4.E help shed light on the origin(s) of these unique characteristics of PCFs with regard to SBS. The simulation results confirm that all four PCFs studied are acoustically highly multimode for the present experimental conditions and have a tendency to behave as antiguides for small core. The wavelength of the acoustic wave, Λ_A, being expressed in terms of the pump optical wavelength, λ, and the core refractive index, n, as $\Lambda_A=\lambda/2n$, the acoustic wavelength was approximately 0.5 μm for the PCFs studied in the experiments at the 1550 nm wavelength (assuming an effective $n=1.444\,02$). This wavelength is indeed much smaller than the core diameter of even the RB65 and the CF and definitely below the cutoff for a single acoustic mode. The multimode acoustic character of these PCFs can explain the higher SBS threshold observed for all of them, including the RB61 with a core of 8 μm. In the case of the small-core CF, diffraction of the acoustic pointlike source, jointly with the acoustic antiguide nature of this small-core fiber, will tend to enhance the spread of the acoustic displacements and decrease the overlap between the optical and acoustic fields, which is likely responsible for the even higher threshold. These features can also explain the drop in the effective value of the product nV_A and the corresponding precipitous drop of the Brillouin shift for small core sizes. As seen in the simulations, the acoustic displacements corresponding to the main Brillouin peak are mostly $u_z(x,y)$ and the acoustic wave therefore mainly longitudinal in character. Moreover, the longitudinal displacements are mainly confined to the core for RB61 and RB65, but extend out into the holey cladding for the CF.

Next, we examine the nature of the acoustic modes giv-

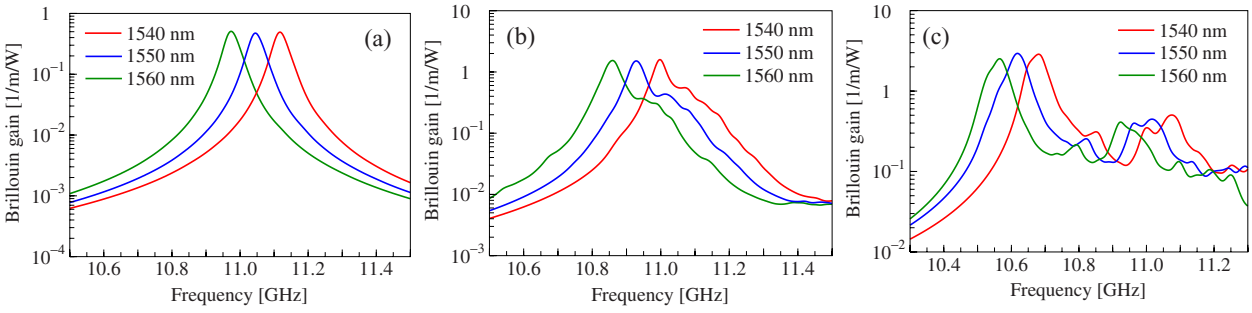

Fig. 15. (Color online) Brillouin gain calculated from Eq. (6) for RB61, RB65, and CF, respectively.

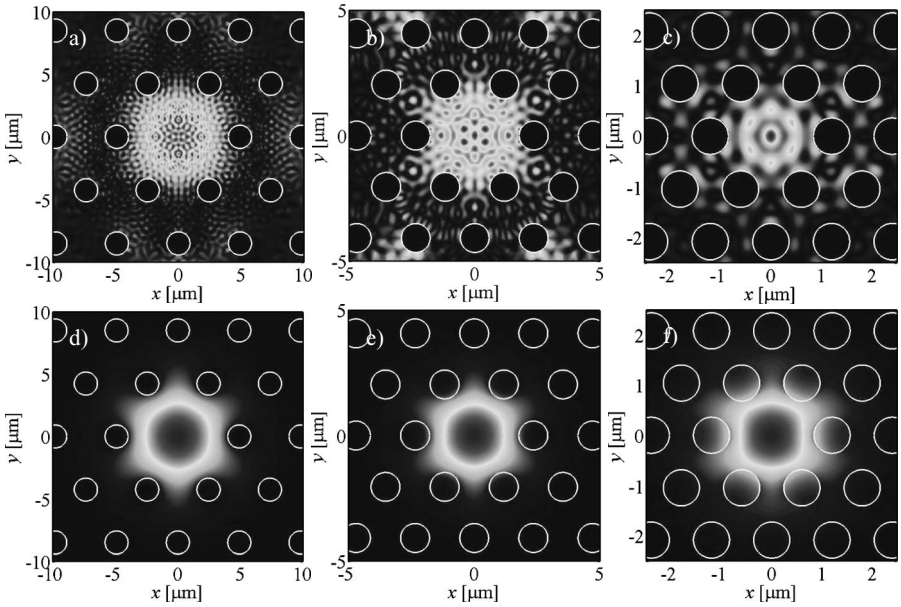

Fig. 16. a)–c) u_z component of the acoustic displacement distribution at the main Brillouin peak frequency, 11.044, 10.920, 10.622 GHz, for RB61, RB65, and CF, respectively. d)–f) Corresponding optical mode field distribution for 1550 nm.

ing rise to the second Brillouin peak observed in the experiment. For the larger-core size RB61, no such peak is observed in either the experimental or the calculated spectrum while, for the smaller-core RB65 and CF, a second peak is observed at a position that is consistent with the calculated BGS. To compare the relative intensities of the peaks in both figures, it is important to recall that the Brillouin intensities go as $I_0 e^G$, where G is the calculated Brillouin gain. Thus, a ratio of 5 and 10 of the magnitudes of different gain peaks will translate in a ratio of 150 and 22 000 of the corresponding Brillouin peak intensities, which are close to the experimentally measured ratios of the main to second peaks intensities in both smaller-core fibers, respectively. For the CF in particular, the measured second peak is indeed quite small when compared to the main peak. The nature of the second peak can be inferred from the acoustic modeling results. As seen in Figs. 16(c) and 16(d) for the CF, the acoustic displacements giving rise to the second peak(s) around 10.82 GHz possess a significant transverse component (see u_x and u_y). The corresponding modes are therefore not purely longitudinal but partially torsional-radial as well. This also explains the lower average acoustic velocity obtained in Fig. 12 for the second peak of the CF (3581 m/s) when compared with that obtained from the main peak. This conclusion is also supported by the results of Bongrand

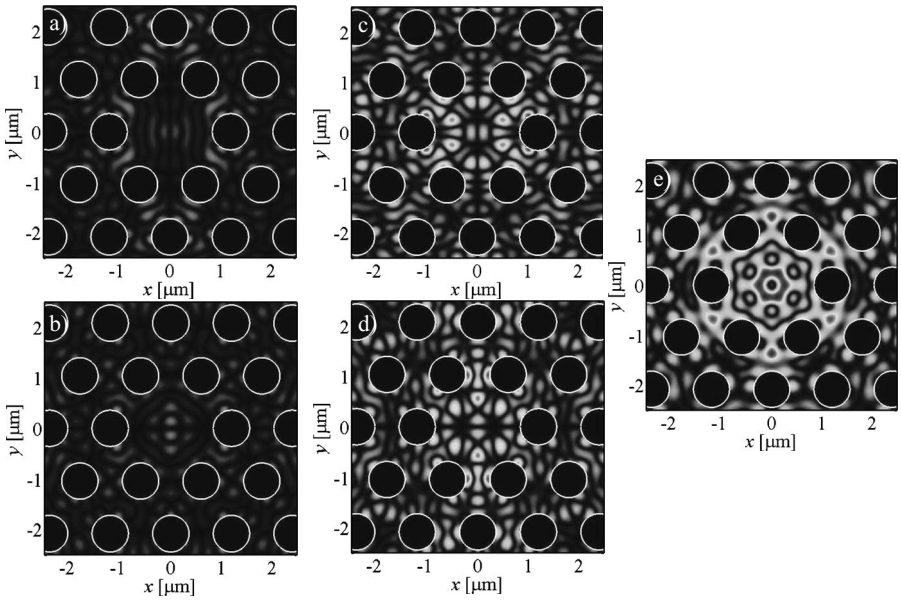

Fig. 17. a) and b) Acoustic displacement distribution components u_x and u_y [u_z in Fig. 16(c)] of CF at the main Brillouin peak frequency, 10.622 GHz. c)–e) Acoustic displacement distribution components u_x, u_y, u_z, respectively, at the third peak frequency, 10.96 GHz.

et al. [14]. The authors of [14] have shown that coupled longitudinal/transverse SBS takes place in long lengths of small-core fibers. They have also shown that this coupled SBS is due to the finite numerical aperture and multimode acoustic character of small core optical fibers, which result in the incident optical beam being scattered at a nonzero angle relative to the fiber axis, and the generation of acoustic waves that can be torsional-radial TR_{2n} or radial R_{0n}. In this process, both longitudinal and several transverse torsional-radial waves can be excited. One of these transverse waves can in fact give rise to forward SBS (also called cladding Brillouin scattering (CBS) or guided wave Brillouin scattering, (GWBS) [15]), while another can affect the regular backward SBS (see below). Although this coupled SBS is only observed for very long lengths of conventional fibers, our results show that the effect can be significantly enhanced in PCFs. This is after all not so surprising, given the elastically soft holey cladding in small-core PCFs with a high air volume fraction, which makes it easy for a longitudinal displacement to be coupled to a transverse or radial one. In crystals, the relevant elastic modulus for such coupled displacements is in fact $(C_{11}-C_{12})$, which is a transverse or shear elastic modulus. In our case, "1" would correspond to the z or longitudinal direction and "2" to the radial direction. This also explains why the line of ν_B versus $1/\lambda$ corresponding to the second peak does not extrapolate to zero. As shown by the calculations of Laude *et al.* [5], transverse acoustic branches extrapolate to zero frequency from large propagation constants β or large radii a of the acoustic waveguide but curve up and intersect the vertical frequency axis at nonzero values and with zero slope in the limit of zero propagation constants or radii. The shape of these branches follows what is called a "hyperbolic dispersion" (see Fig. 2 in Ref. [12]) and the intersection at $\beta a=0$ with the frequency axis is called the cut-off frequency. The acoustic waves at this cut-off frequency are of purely radial character.

The nature of the third peak, only observed in our experiment for the smallest-core CF, can be interpreted in two different ways. By comparing the experimental and the calculated spectrum, one notes that the calculated BGS in Fig. 15 exhibits features at approximately the same frequency, where the third peak is observed in the experimental spectrum, i.e., 400 MHz above the main peak. One could therefore attribute the latter to higher-order modes, of a mixed longitudinal/torsional-radial character, in a similar way as for the second peak. However, we have seen that such modes are characterized by lower acoustic velocities than the purely longitudinal modes that give rise to the main peak and that the average acoustic velocity of the modes corresponding to the third peak is relatively close to that of the longitudinal modes corresponding to the main peak. We therefore favor an alternative interpretation, which is consistent with the results of the study by Bongrand *et al.* [14], and one that should, in general, be specific to small-core PCFs. This interpretation is based on three characteristics of small-core PCFs. First, as noted above, the small core of these fibers results in the SBS-generated acoustic waves being diffracted out into the holey cladding as from a pointlike source, an effect that is reinforced by their acoustic antiguiding nature. Second, the strong diffraction and soft holey cladding enhances the coupling between longitudinal and transverse waves (see shear modulus $C_{11}-C_{12}$), the latter waves being mostly radial in character for small-core and/or short wavelengths. Finally, the stiffer solid outer cladding that bounds the soft holey inner cladding can reflect radial waves very effectively. These three characteristics point to the soft inner holey cladding acting as a resonant cavity and preferentially amplifying a particular radial mode cogenerated with the longitudinal modes. Because the whole SBS process is coherent, i.e., phase matched, this resonant radial mode can modulate the backward propagating Stokes wave through electrostriction, giving rise to a new peak, our third peak. The physical validity of such an explanation can be tested by estimating the size of the resonant cavity, d, from the formula $\Delta\nu=V_A/d$ in which $\Delta\nu \sim 400$ MHz is the measured frequency shift between the main and third peak and $V_A=5259$ m/s is the acoustic velocity estimated from the wavelength dependence of the third peak Brillouin shift. From this formula, the size of the resonant cavity is found to be $d\sim 13$ μm, which is quite close to the radius of the holey cladding of the CF, 10.4 or 12 μm, depending on the symmetry direction chosen in the hexagonal cross section. One should note that a transverse resonant mode will have two nodes in such a fiber, one at the center of the fiber and the other at the interface between the holey inner cladding and the solid outer cladding, so that the observed modulation frequency of the Stokes wave (400 MHz) should in fact be double the frequency of the resonant radial acoustic mode. It is worth mentioning that the explanation given above for the third peak observed in the CF also appears to be consistent with the recent forward SBS result of a time-resolved pump-probe experiment by Dainese *et al.* [16], in which a pulsed pump in a small-core PCF was shown to be exciting an acoustic wave through SBS, which then modulated the intensity of a circularly polarized cw probe for approximately 10 ns, i.e., a typical lifetime for an acoustic mode.

In closing, we also note the strong polarization dependence observed in the RB65 and CF. This polarization dependence reveals the significant birefringent character of small-core PCFs. No such birefringence was observed in the larger-core RB61 fiber. Detailed measurements of the polarization dependence of SBS in the PCFs studied and a comparison with an elliptical core fiber will be published elsewhere in the near future.

6. CONCLUSIONS

In the present study, we have reported experimental and modeling results on SBS in several PCFs with decreasing core size. These results reveal the presence of two or three peaks in the spectrum, each of which corresponds to a multiplicity of acoustic modes (multimode acoustic character of PCFs). The main peak, at lower frequency, is clearly due to longitudinal acoustic modes guided in the core. Transverse or torsional-radial modes are also excited, which are responsible for a second peak at a slightly higher frequency (~100 MHz). This interpretation is confirmed by the x and y components of the displacement dis-

tribution obtained in the simulations. As the core size decreases, the frequencies of the longitudinal and torsional-radial acoustic modes drop precipitously and the SBS threshold increases faster than expected for conventional SMFs. Both observations can be attributed to diffraction of the acoustic wave out of the small-core and the antiguiding character of PCFs. For an even smaller-core PCF, a third peak is also observed, which yields an acoustic velocity that is only slightly lower than that of the main longitudinal mode. This third peak results from the modulation of the main Stokes wave by either torsional-radial or radial modes, resonating within an elastically deformable holey cladding cavity. Finally, SBS in small-core PCFs exhibits a strong polarization dependence.

ACKNOWLEDGMENTS

Special thanks go to Ryan Bise and David Di Giovanni, of OFS, Inc., who supplied the two RB fibers studied, and Cato Fagermo from Crystal Fiber, Inc. for the smallest-core PCF. We have also benefited from extensive scientific discussions with Francis Ndi. This work was supported by the National Science Foundation under grant ECS-0401269 and by the Center for Optical Technologies at Lehigh University, which is funded by the State of Pennsylvania Department of Community and Economic Development.

REFERENCES

1. J. Toulouse, E. J. H. Davies, S. Y. Texier, R. K. Pattnaik, L. Farr, B. J. Mangan, and J. C. Knight, "Stimulated Brillouin scattering and lasing," in *Nonlinear Guided Waves and Their Applications*, edited by A. Sawchuk, Vol. **80** of OSA Trends in Optics and Photonics (Optical Society of America, 2002), paper PD7.
2. L. Zou, X. Bao, and L. Chen,"Brillouin scattering spectrum in photonic crystal fiber with a partially germanium-doped core," Opt. Lett. **28**, 2022–2024 (2003).
3. P. Dainese, P. St. J. Russell, N. Joly, J. C. Knight, G. S. Wiederhecker, H. L. Fragnito, V. Laude, and A. Khelif, "Stimulated Brillouin scattering from multi-GHz-guided acoustic phonons in nanostructured photonic crystal fibers," Nat. Phys. **2**, 388–923 (2006).
4. K. Saitoh and M. Koshiba, "Numerical modeling of photonic crystal fibers," J. Lightwave Technol. **23**, 3580–3590 (2005).
5. V. Laude, A. Khelif, S. Benchabane, M. Wilm, T. Sylvestre, B. Kibler, A. Mussot, J. M. Dudley, and H. Maillotte, "Phononic band-gap guidance of acoustic modes in photonic crystal fibers," Phys. Rev. B **71**, 45107-1–45107-6 (2005).
6. G. P. Agrawal, *Nonlinear Fiber Optics* (Academic, 1995).
7. D. Cotter, "Observation of stimulated Brillouin scattering in low-loss silica fibre at 1.3 μm," Electron. Lett. **18**, 495–496 (1982).
8. A. Yeniay, J.-M. Delavaux, and J. Toulouse, "Spontaneous and stimulated Brillouin scattering gain spectra in optical fibers," J. Lightwave Technol. **20**, 1425–1432 (2002).
9. J. F. Berret and M. Meissner, "How universal are the low temperature acoustic properties of glasses?," Z. Phys. B: Condens. Matter **70**, 65–72 (1988).
10. J. Yu, B. Kwon, and K. Oh, "Analysis of Brillouin frequency shift and longitudinal acoustic wave in a silica optical fiber with a triple-layered structure," J. Lightwave Technol. **21**, 1779–1786 (2003).
11. I. Enomori, K. Saitoh, and M. Koshiba, "Fundamental characteristics of localized acoustic modes in photonic crystal fibers," IEICE Trans. Electron. **E88**, 876–881 (2005).
12. A. Kobyakov, S. Kumar, D. Q. Chowdhury, A. B. Ruffin, M. Sauer, and S. R. Bickham, "Design concept for optical fibers with enhanced SBS threshold," Opt. Express **13**, 5338–5346 (2005).
13. K. Saitoh and M. Koshiba, "Full-vectorial imaginary-distance beam propagation method based on a finite element scheme: application to photonic crystal fibers," IEEE J. Quantum Electron. **38**, 927–933 (2002).
14. I. Bongrand, E. Picholle, and C. Montes, "Coupled longitudinal and transverse stimulated Brillouin scattering in single-mode optical fibers," Eur. Phys. J. D **20**, 121–127 (2002).
15. R. M. Shelby, M. D. Levenson, and P. W. Bayer, "Guided acoustic-wave Brillouin scattering," Phys. Rev. B **31**, 5244–5252 (1985).
16. P. Dainese, P. St. J. Russell, G. S. Wiederhecker, N. Joly, H. L. Fragnito, V. Laude, and A. Khelif, "Raman-like scattering from acoustic phonons in photonic crystal fiber," Opt. Express **14**, 4141–4150 (2006).